

Numerical simulation for a rising bubble interacting with a solid wall: impact, bounce, and thin film dynamics

Changjuan Zhang,^{1,2} Jie Li,³ Lishi Luo,^{1,4} and Tiezheng Qian^{2, a)}

¹⁾Beijing Computational Science Research Center, Beijing 100193, China

²⁾Department of Mathematics, Hong Kong University of Science and Technology, Clear Water Bay, Kowloon, Hong Kong

³⁾BP Institute and Department of Engineering, University of Cambridge, Cambridge CB3 0EZ, United Kingdom

⁴⁾Department of Mathematics & Statistics, Old Dominion University, Norfolk, VA 23529, USA

(Dated: 14 November 2018)

Using Arbitrary Lagrangian-Eulerian method on an adaptive moving unstructured mesh, we carry out numerical simulations for a rising bubble interacting with a solid wall. Driven by the buoyancy force, the axisymmetric bubble rises in a viscous liquid toward a horizontal wall, with impact on and possible bounce from the wall. First, our simulation is quantitatively validated through a detailed comparison between numerical results and experimental data. We then investigate the bubble dynamics which exhibits four different behaviors depending on the competition among the inertial, viscous, gravitational, and capillary forces. A phase diagram for bubble dynamics has been produced using the Ohnesorge number and Bond number as the two dimensionless control parameters. Finally, we turn to the late stage of the bubble rise characterized by a small flux of liquid escaping from the thin film between the wall and bubble. Since the thin film dynamics can be accurately described by the lubrication approximation, we carry out numerical simulations to compare the simulation results with the predictions of the lubrication approximation. Remarkable agreement is obtained to further demonstrate the accuracy of the simulations.

Keywords: Rising bubble, Bouncing, Film drainage, Adaptive moving mesh, ALE method, Ohnesorge number.

I. INTRODUCTION

The interaction of a bubble or droplet with a solid surface occurs in a variety of industrial and natural processes^{1,2}. Many experimental, numerical, and theoretical studies have been carried out in past years, yet there are still problems related to bubble-wall collision that are not fully understood. The purpose of the present work is to numerically investigate the interaction between a rising bubble and a horizontal solid wall above.

Three major processes have been simulated in our study. First, the bubble accelerates from where it is released and quickly reaches a steady state of rising in which the bubble shape and velocity remain constant. Then there is the bouncing process with the bubble impact on and bounce from the wall. Finally there is the thin film drainage process in which the bubble slowly squeezes the liquid film between the wall and bubble.

For the first process, i.e., the rise of a bubble in a liquid, most of the studies focused on the terminal velocity and bubble deformation. Duineveld³ experimentally studied the rising velocity and bubble shape in pure water at high Reynolds number. Wu et al.⁴ reported experimental studies on the shape and path of small air bubbles rising in clean water.

Regarding the dynamics of bouncing process, the inter-

action between a rising bubble and a horizontal wall has been studied extensively over the past decades. Tsao and Koch⁵ observed a bubble bouncing from a horizontal wall by using a high-speed camera. Klaseboer et al.⁶ studied the rebound of a drop impinging on a wall both experimentally and numerically. Legendre et al.⁷ and Zenit et al.⁸ studied a bubble bouncing from a solid wall in a viscous liquid experimentally. Recently, Kosior et al.⁹ reported the influence of n-octanol on the bubble impact velocity and bouncing from hydrophobic surfaces experimentally. Qin et al.¹⁰, Albadawi et al.¹¹, Klaseboer et al.¹², and Manica et al.¹³ theoretically and numerically studied the bubble rise, impact, and bounce processes. The film drainage process was investigated in Ref. 6 experimentally and in Ref. 10 numerically. In addition, bubbles interacting with fluid-fluid interfaces were also studied in many works¹⁴⁻¹⁶.

There have been many theoretical and numerical works on the dynamics of a bubble or drop approaching a solid surface. Yiantsios et al.¹⁷ analyzed the buoyancy-driven motion of a drop towards a solid surface or a deformable interface using the lubrication theory and boundary-integral theory. Power¹⁸ studied the interaction of a deformable bubble with a rigid wall at small Reynolds number. Based on an earlier work⁶, Klaseboer et al.¹² successfully predicted the bubble trajectory and thin film drainage by using a force balance model. The terminal velocity of a rising bubble has been noted to be an important factor in bubble dynamics^{3,4,19}. A number of numerical methods have been used for solving the multiphase flow problems, including Volume of

^{a)} Author to whom correspondence should be addressed: maqian@ust.hk.

Fluid (VOF) method^{11,16,20}, front tracking method²¹, level set method^{22,23}, and phase field method²⁴. A mass-conserving lattice Boltzmann method, which is a diffuse interface model, was proposed by Fakhari et al.²⁵. The above methods are non-conforming methods, i.e., the interface is not composed of lines in the mesh.

The Arbitrary Lagrangian-Eulerian (ALE) method is an interface conforming method with the interface being composed of lines in the mesh. Étienne et al.²⁶ simulated the free surface flow of a viscoelastic material by using the ALE method. Hu²⁷ and Hu et al.²⁸ carried out direct numerical simulations of fluid-solid systems using the ALE technique. Yue et al.²⁹ simulated bubble growth in polymer foaming using the ALE method. Qin et al.¹⁰ numerically investigated the interaction of a rising bubble with a solid wall using the ALE method. In this work, they considered large Bond number (Bo) which leads to large bubble deformation. In addition, the three modes they presented in a phase diagram are mostly in the overdamped regime.

In the present work, we consider small Bond number with limited bubble deformation, with a focus on the transition between underdamped and overdamped bubble dynamics. On the one hand, our simulations are able to accurately capture the oscillatory behaviors of the bubble in the underdamped regime. On the other hand, our simulations are able to achieve quantitative agreement with the prediction of lubrication approximation for the thin film between the wall and bubble in the late stage of the bubble rise. Our numerical simulations are carried out using the ALE method. We track the interface explicitly to allow accurate application of boundary conditions at the interface. Finite element method employing an adaptive unstructured triangulation method is applied. Further details on the numerical method used in the present work can be found in Ref. 30.

The paper is organized as follows. In section 2, we present the governing equations with boundary conditions and the numerical method applied here. In section 3, we present the validation of numerical simulation through a comparison with experimental data. In section 4, we present the numerical results for the transition between underdamped and overdamped bubble dynamics. Four distinct regimes of bubble dynamics are identified and a phase diagram is produced using the Ohnesorge number (Oh) and Bo as the two control parameters. In section 5, we present the numerical results showing quantitative agreement with the prediction of lubrication approximation for the thin film dynamics in the late stage of the bubble rise. The paper is concluded in section 6.

II. MATHEMATICAL FORMULATION

A. Governing equations and boundary conditions

Consider a gas bubble that is driven by buoyancy force and rises in a liquid toward a horizontal wall. We assume

that the fluids are Newtonian, the interfacial tension is uniform, and the flows are incompressible. The governing equations are given by

$$\begin{cases} \nabla \cdot \mathbf{u} = 0, \\ \rho \left(\frac{\partial \mathbf{u}}{\partial t} + \mathbf{u} \cdot \nabla \mathbf{u} \right) = \rho \mathbf{g} - \nabla p \\ \quad + \nabla \cdot \{ \mu (\nabla \mathbf{u} + \nabla \mathbf{u}^T) \} + T, \end{cases} \quad (1)$$

where \mathbf{u} is the flow velocity, the density ρ is a constant in each phase, t is the time, \mathbf{g} is the gravitational acceleration, p is the pressure, μ is the shear viscosity, and $T = -\sigma(\nabla \cdot \mathbf{n})\mathbf{n}\delta$ is the capillary force density. Here σ denotes the gas-liquid interfacial tension, \mathbf{n} is the interfacial normal vector, and δ is the surface Dirac function which is non-zero at the gas-liquid interface.

For the axisymmetric dynamics, the governing equation (1) can be written in cylindrical coordinates with $(r, \theta, z) \in \Omega$, where Ω is the flow domain. Under the assumption of axisymmetry, the continuity equation is

$$\frac{1}{r} \frac{\partial}{\partial r}(ru) + \frac{\partial v}{\partial z} = 0 \quad (2)$$

and the momentum equation is given by

$$\begin{aligned} \rho \frac{du}{dt} = & -\frac{\partial p}{\partial r} + \frac{1}{r} \frac{\partial}{\partial r} \left(r \left(2\mu \frac{\partial u}{\partial r} \right) \right) \\ & + \frac{\partial}{\partial z} \left(\mu \left(\frac{\partial v}{\partial r} + \frac{\partial u}{\partial z} \right) \right) - \frac{2\mu u}{r^2}, \end{aligned} \quad (3)$$

$$\begin{aligned} \rho \frac{dv}{dt} = & -\frac{\partial p}{\partial z} + \frac{1}{r} \frac{\partial}{\partial r} \left(r\mu \left(\frac{\partial v}{\partial r} + \frac{\partial u}{\partial z} \right) \right) \\ & + \frac{\partial}{\partial z} \left(2\mu \frac{\partial v}{\partial z} \right) + \rho g, \end{aligned} \quad (4)$$

where u and v are the radial (r) and axial (z) velocity components. The boundary condition applied at the gas-liquid interface Γ is a natural condition expressing the force balance between the interfacial tension and stress:

$$[(-p\mathbf{I} + \mu\mathbf{D} \cdot \mathbf{n})]_{\pm}^{\pm} = \sigma\kappa\mathbf{n}, \quad (5)$$

where $[\cdot]_{\pm}^{\pm}$ denotes the difference between the physical quantity on the two sides of the interface,

$$\mathbf{D} = \begin{bmatrix} 2u_r & u_z + v_r \\ u_z + v_r & 2v_z \end{bmatrix} \quad (6)$$

is the strain rate tensor, and κ the curvature. We consider a gas that is incompressible and maintained at a constant pressure p_0 (which can be assumed to be 0), with density and viscosity being zero.

The interface moves with the fluid velocity. As a result, the interface motion is described by the kinematic boundary condition

$$\frac{d\mathbf{x}}{dt} = \mathbf{u}(\mathbf{x}), \quad (7)$$

where $\mathbf{x} = (x, y, z)$ denotes the position of a point on the interface.

B. Numerical method

The numerical method used in this study has been presented in Ref. 26 and 30. It is suitable for solving two-dimensional and axisymmetric three-dimensional Stokes and Navier-Stokes equations. Below is an outline of the method.

There have been many excellent mesh generators, e.g. BAMG³¹, Triangle³², and GRUMP³³. These generators prescribe the position of a boundary but not the vertices on it. An adaptive mesh generator was described in Ref. 30 where the interfaces between different phases are lines of the mesh system, and the triple junction points (if any) are mesh nodes. The interfacial motion can be tracked by adapting mesh to the shape of the interfaces. The mesh can be generated by the following algorithm:

1. The motion of the vertices at the interfaces is determined by its velocity. The Laplacian smoothing technique is used to relocate the vertices not at the interfaces.
2. Edges not at the interfaces are swapped according to the Delaunay condition.
3. Edge splitting/contraction is used to refine or coarsen the mesh.

The adaptive unstructured mesh is very flexible and can fit around nearly all geometries. Figure 1 illustrates the unstructured mesh at some time instant in the present work.

An Arbitrary Lagrangian-Eulerian (ALE) method is employed, which combines the advantages of both Lagrangian and Eulerian methods and alleviate the drawbacks. Dynamic boundary conditions at the interfaces can be incorporated naturally and accurately in a finite element method (FEM). Combining ALE with FEM, the weak form of the continuity equation and momentum equation can be discretized on a finite element triangulation. Augmented Lagrangian technique with a Uzawa method is used to exactly enforce the zero divergence of velocity. The SPOOLES (Sparse Object Oriented Linear Equations Solver) is used as a linear solver.

III. VALIDATION OF NUMERICAL SIMULATION

Here we consider a bubble that rises in a liquid toward a horizontal solid surface with a high velocity due to the large buoyancy force. In this dynamic regime, the bubble may repeatedly bounce from the solid surface with oscillatory deformation during the process of alternate rise and bounce.

There exist several approaches to the investigation of this phenomenon. A model based upon force balance has been presented by Manica et al.¹³. Numerical simulation based on the volume of fluid (VOF) method has been presented by Albadawi et al.¹¹. These two works

compared their numerical results with the experimental data of Kosior et al.⁹. In the present work, in order to validate our numerical method and demonstrate its advantage, we carry out a simulation for exactly the same case: a gas bubble of diameter $D = 1.48$ mm is released deep in the water and reaches its terminal velocity before the first impact on the solid surface. In this case study, the Ohnesorge number is 0.0031 and the Bond number is 0.298.

The bubble is released with an initial velocity equal to zero. Then the velocity increases with a decreasing acceleration until the terminal velocity is reached. Given the high terminal velocity, the bubble motion is characterized by alternate rise and bounce. The oscillatory variation of the bubble velocity, defined as the velocity at the centroid of the bubble, is plotted in Figure 2. The dashed line represents the data extracted from the experimental work by Kosior et al.⁹, the dash-dotted line represents the computational results of Albadawi et al.¹¹, and the solid line represents the computational results in the present work. It is readily seen that our simulation results show a quantitative agreement with the experimental data.

The terminal velocity in our simulation is ≈ 348 mm/s, which agrees with the experimental value very well, with a relative discrepancy about 0.5%. Distinct “approach-bounce” cycles are clearly seen. In addition, high frequency oscillations can be observed in the first two increasing stages of the velocity variation. This is neither an experimental nor a numerical artifact but a reality because the very small Ohnesorge number here leads to a number of sub-oscillations. Physically, a very small Oh means the viscous damping is very weak and oscillations may exist at different scales due to the joint effect of inertia and interfacial tension. The time scale for oscillation and that for velocity damping are measured relative to each other in the dimensionless parameter Oh, which will be explained in subsection IV A.

The oscillatory variation of the aspect ratio of the bubble is shown in Figure 3, in which our numerical results are compared with the numerical results of Albadawi et al. and the experimental results of Kosior et al.. Here the aspect ratio is defined as $R_A = d_h/d_v$, where d_h is the maximum extent of the bubble in the horizontal direction and d_v is the maximum extent of the bubble in the vertical direction.

Our simulation results are good for both the bubble velocity and aspect ratio. This is particularly seen when the sub-oscillations at shorter time scale are concerned. The dynamics at low Oh is more complicated because viscous damping is weak and oscillations arise from the joint effect of inertia and interfacial tension. Furthermore, the high impact speed will lead to the excitation of high frequency oscillation modes. In fact, when the impact speed is low (with the bubble released not far from the solid surface), no high frequency oscillation mode is observed. Physically, an oscillation requires the inertia to take effect. A high frequency oscillation mode occurs at a small length scale that is smaller than the bubble

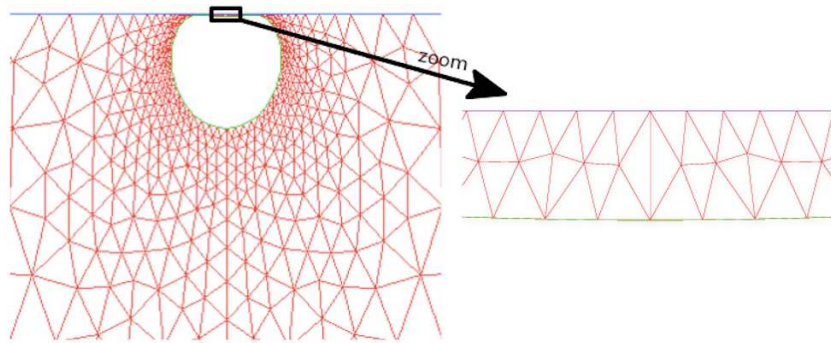


FIG. 1. An illustration of adaptive mesh.

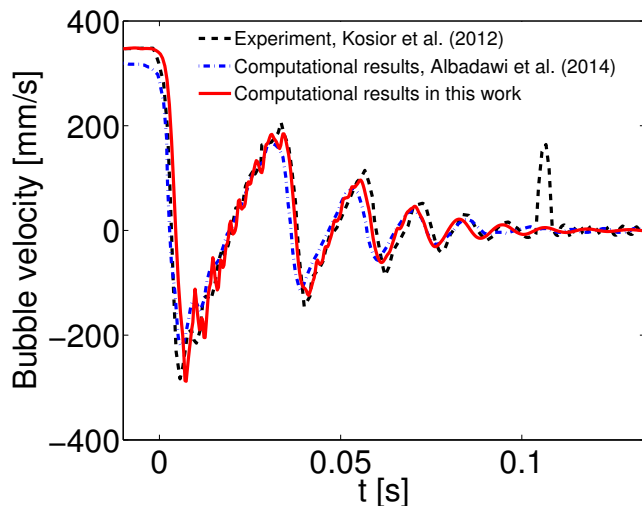


FIG. 2. The oscillatory time variation of the bubble velocity. Here we make comparison with the numerical results (dash-dotted line) from Albadawi et al. (2014) and the experimental results (dashed line) from Kosior et al. (2012). The terminal velocity in our simulation is ≈ 348 mm/s, in good agreement with the experimental value.

size. To have a sufficiently large Re number at the small length scale, a large velocity is required. Therefore, the high frequency modes only appear at small Oh with high impact speed.

In Figure 4, the interfaces from our simulation (red solid lines) are superimposed on the pictures from Ref. 9 at different times during the first and second collisions and after bouncing. The upper row of each sequence shows top-view photos, which clearly display the variation of the diameter of the liquid film. The lower row of each sequence shows the shape and position of the bubble. It is clearly seen that our numerical results are in good agreement with the experimental results. The bubble hits the wall for the first time with the terminal velocity which is high. As a result, during the collision and rebound, the oscillatory deformation of the bubble is strong. The approaching velocity for the second col-

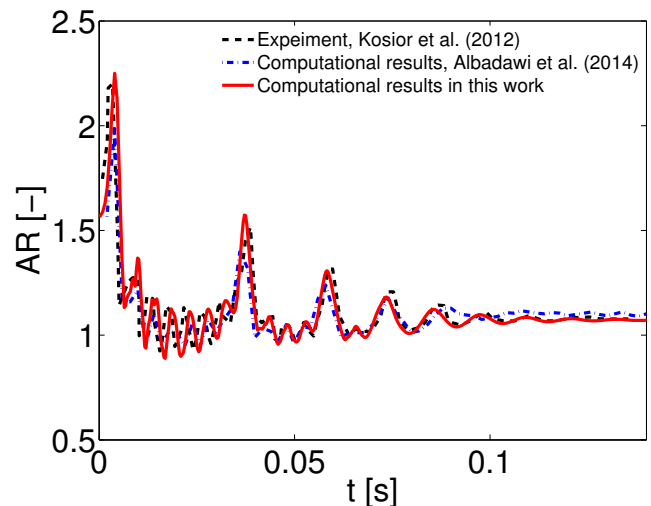


FIG. 3. The oscillatory variation of the aspect ratio of the bubble. Here we make comparison with the numerical results (dash-dotted line) from Albadawi et al. (2014) and the experimental results (dashed line) from Kosior et al. (2012).

lision is smaller than the terminal velocity, leading to a weaker oscillatory deformation of the bubble than in the first collision. Finally, the bubble acquires a fixed shape with a thinning liquid film between the bubble and the solid surface.

IV. DYNAMIC PHASE DIAGRAM

A. Control parameters

The dynamics of bubble can exhibit different behaviors depending on the competition among the inertial, viscous, gravitational, and capillary forces. In addition to the density and viscosity ratios, the two most important dimensionless parameters are the Bond number and Ohnesorge number. The Bond number measures the gravitational force relative to the interfacial tension force,

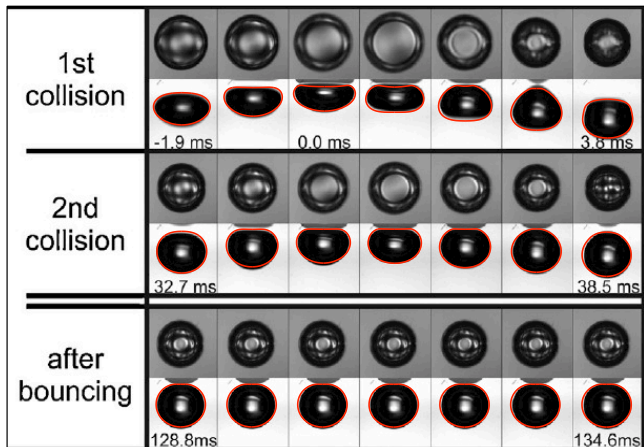


FIG. 4. The interfaces from our simulation (red solid lines) are superimposed on the pictures from Kosior et al.⁹ at different times during the first and second collisions and after bouncing. Here, due to the difference (≈ 1 ms) between the experimental data and our numerical results for oscillation period (≈ 34.6 ms), there will be accumulated difference after a few cycles. Therefore, to optimize the comparison for bubble shapes, we have adjusted the initial time instants for the 1st and 2nd collisions, respectively. We have checked the numerical convergence in determining the oscillation period. The small relative difference between the experimental data and our numerical results ($\approx 3\%$) may be caused by the small uncertainty in physical parameters, e.g. bubble diameter and interfacial tension.

given by

$$\text{Bo} = \frac{\Delta\rho g D^2}{\sigma},$$

where $\Delta\rho$ is the difference between the liquid and gas densities, g is the gravitational acceleration, D is the characteristic length (i.e., the diameter of the bubble in spherical shape), and σ is the interfacial tension. The Bond number can be used to characterize the shape of a bubble moving in a surrounding liquid, with a larger Bo leading to a bigger deformation of bubble shape.

The Ohnesorge number measures the viscous force relative to the inertial and interfacial tension forces, defined by

$$\text{Oh} = \frac{\mu}{\sqrt{\rho\sigma D}}.$$

where μ is the shear viscosity, ρ is the liquid density, and σ and D are the same as above. Physically, this dimensionless parameter can be understood as a ratio of two time scales: (i) the time scale for oscillation $\tau_{osc} \sim \sqrt{\rho D^3/\sigma}$ determined by the inertial and interfacial tension forces, and (ii) the time scale for velocity relaxation $\tau_{rel} \sim \rho D^2/\mu$ determined by the inertial and viscous forces, with $\text{Oh} = \tau_{osc}/\tau_{rel}$. If τ_{osc} is much smaller than τ_{rel} , then Oh is small, the viscous damping is weak, and oscillatory behaviors may occur.

B. Four regimes of bubble dynamics

In our simulations, the liquid water is confined in an enclosed tube with 200 mm in height and 80 mm in diameter. A spherical gas bubble of diameter $D \sim 1$ mm is released from the bottom of the tube. The flow is assumed to be axisymmetric and a cylindrical coordinate system with coordinates r and z is used. Accordingly, our computational domain is $[0, 40] \times [-200, 0]$, with the origin located at the center of the upper surface of the tube. The center of the bubble is initially located at $(r_0, z_0) = (0, -180)$, which is deep enough for the bubble to reach the terminal velocity before hitting the upper wall.

We fix $\rho = 1000$ kg/m³ for liquid density and use different values for bubble diameter D , viscosity μ , and interfacial tension σ in our simulations. Different combinations of D , μ , and σ will give rise to different dynamic behaviors of the bubble which rises and approaches the upper wall and then may or may not bounce. The terminal velocity plays an important role in controlling the bubble dynamics. Higher the terminal velocity is, more easily and probably the bubble bounces. Therefore, we release the bubble far away from the upper wall to make sure that the bubble reaches its terminal velocity in all the simulations reported in this work.

Four distinct dynamic regimes have been observed in a large number of numerical simulations. Figure 5 illustrates the four regimes by plotting the bubble positions for four different cases. The red curves represent the positions of the center of the upper gas-liquid interface and the blue curves represent the positions of the center of the lower gas-liquid interface. The four dynamic regimes are illustrated by four sub-figures as follows. In figure 5(a), the upper and lower interfaces both show oscillatory positions, and this regime is called the regime of absolute bouncing; in figure 5(b), the upper interface slowly and monotonically approaches the wall without oscillation while the lower interface still shows an oscillatory position, and this regime is called the regime of marginal bouncing; in figure 5(c), the upper interface slowly and monotonically approaches the wall without oscillation while the lower interface shows a non-monotonic yet non-oscillatory behavior, and this regime is called the regime of marginal overdamping; in figure 5(d), the upper and lower interfaces both slowly and monotonically approach the wall without oscillation, and this regime is called the regime of absolute overdamping. Here we mention that the validation case in section III is in the regime of absolute bouncing.

In figure 6, the four dynamic regimes are separated in a two-dimensional plot, in which the horizontal axis is μ and the vertical axis is $\sqrt{\rho\sigma D}$. The three straight lines, all passing through the origin, are used to indicate the separation of four regimes. Note that $\text{Oh} = \mu/\sqrt{\rho\sigma D}$ is a constant along each line. Therefore, figure 6 implies that the four dynamic regimes are predominantly separated by Oh, which becomes smaller toward the upper left part

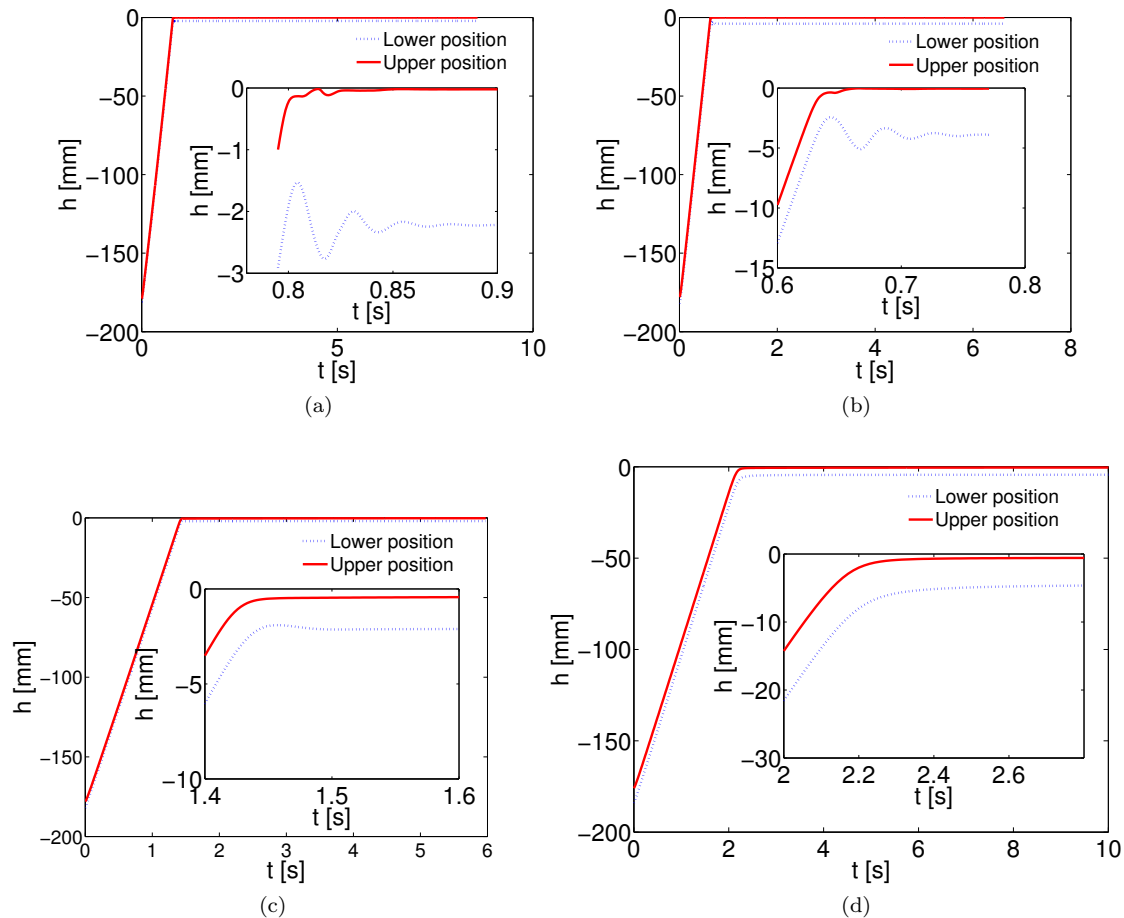


FIG. 5. Four dynamic regimes are identified for the bubble which rises and approaches the upper wall and then may or may not bounce. Here the red (blue) curves represent the positions of the center of the upper (lower) gas-liquid interface. (a) Absolute bouncing: the upper and lower interfaces both show oscillatory positions. (b) Marginal bouncing: the upper interface slowly and monotonically approaches the wall without oscillation while the lower interface still shows an oscillatory position. (c) Marginal overdamping: the upper interface slowly and monotonically approaches the wall without oscillation while the lower interface shows a non-monotonic yet non-oscillatory behavior. (d) Absolute overdamping: the upper and lower interfaces both slowly and monotonically approach the wall without oscillation.

and larger toward the lower right part. It is readily seen that at very small Oh , the viscous force is too weak to suppress the oscillation which is a joint effect of inertial and interfacial tension forces. As a result, the bubble is likely to bounce. At large Oh , however, the viscous dissipation is strong enough for the bubble to enter the overdamped regime where oscillation is impossible.

C. Phase diagram

Besides Oh , the Bond number Bo is also expected to play a role in controlling bubble dynamics because it controls the deformation of bubble shape. A larger Bo leads to larger deformation. As a result, the effective length scale is made larger than the original and nominal diameter D , and hence the effective Oh is made smaller than the nominal Oh calculated using D . Physically, this

smaller effective Oh makes oscillation more likely to occur. This trend can be observed in Figure 7, which shows that a bubble is more likely to oscillate as Bo is increased and Oh is fixed at a relatively small value. In addition, Bo also controls the terminal velocity and hence the kinetic energy of impact by which oscillatory modes may be excited.

V. THIN FILM DYNAMICS

Both experiments and simulations show that after the “approach-bounce” cycles (if any) are finished, the bubble is very close to the wall and its rise is extremely slow. The dynamics in this regime is dominated by a balance between the buoyancy force due to the gravity and the lubrication force due to the liquid film between the wall and bubble. Physically, the late stage of the bubble rise

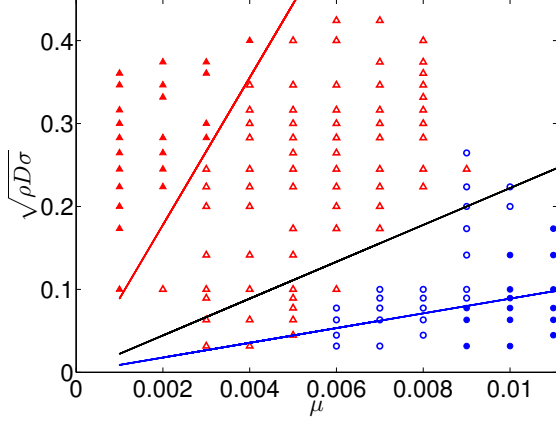


FIG. 6. The four dynamic regimes identified in figure 5 are separated in a two-dimensional plot, with the horizontal axis given by μ and the vertical axis given by $\sqrt{\rho\sigma D}$. The solid triangles are in the regime of absolute bouncing, the hollow triangles are in the regime of marginal bouncing, the hollow circles are in the regime of marginal overdamping, and the solid circles are in the regime of absolute overdamping. The indicative straight lines all pass through origin. Along each line, $\text{Oh} = \mu/\sqrt{\rho\sigma D}$ is a constant.

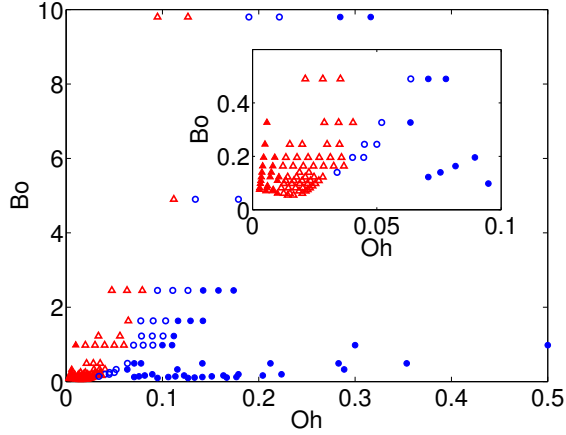


FIG. 7. A phase diagram showing the control by the dimensionless parameters Oh and Bo . The symbols are the same as in figure 6

is characterized by a small flux of liquid escaping from the thin film whose dynamics can be accurately described by the lubrication approximation³⁴. In this section, we carry out numerical simulations to compare the simulation results with the predictions of the lubrication approximation. Remarkable agreement is obtained to further demonstrate the accuracy of the simulations.

A. Lubrication approximation

Assuming the flow to be axisymmetric, we use the cylindrical coordinates r and z with the origin located at the center of the upper wall. Let $h(r, t)$ denote the thickness of the liquid film between the upper wall and the bubble. The rising velocity of the upper gas-liquid interface is given by

$$w(r, t) = -\frac{\partial h(r, t)}{\partial t}, \quad (8)$$

as a function of r and t . At each r , there is a liquid flux escaping from the film, given by the continuity equation

$$\int_0^r 2\pi\tilde{r}w(\tilde{r}, t)d\tilde{r} = 2\pi rh(r, t)\bar{u}(r, t), \quad (9)$$

in which $\bar{u}(r, t)$ is the h -averaged radial velocity at r , define by

$$\bar{u}(r, t) = \frac{1}{h(r, t)} \int_{-h(r, t)}^0 u(r, z, t)dz, \quad (10)$$

in which $u(r, z, t)$ is the radial velocity. We then have

$$\bar{u}(r, t) = \frac{\int_0^r \tilde{r}w(\tilde{r}, t)d\tilde{r}}{rh(r, t)}. \quad (11)$$

Since the liquid layer is thin and $h(r, t)$ varies slowly with r , the equation governing the slow flow becomes

$$\mu \frac{\partial^2 u}{\partial z^2} = \frac{\partial p}{\partial r}, \quad (12)$$

where $\partial p/\partial r$ is independent of z under the lubrication approximation. Solving equation (12) with the boundary conditions $u|_{z=0} = 0$ on the solid surface and $\frac{\partial u}{\partial z}|_{z=-h} = 0$ on the gas-liquid interface, we have

$$u(r, z, t) = \frac{1}{2\mu} \frac{\partial p}{\partial r} (z^2 + 2hz). \quad (13)$$

Combining equations (10) and (13), we obtain

$$\bar{u}(r, t) = -\frac{1}{3\mu} \frac{\partial p(r, t)}{\partial r} h^2(r, t). \quad (14)$$

We then obtain

$$\frac{\partial p(r, t)}{\partial r} = -\frac{3\mu \int_0^r \tilde{r}w(\tilde{r}, t)d\tilde{r}}{rh^3(r, t)} \quad (15)$$

from equations (11) and (14).

In the simplest case of $h(r, t) = h(t)$ being independent of r , p can be expressed as

$$p(r, t) = \frac{3\mu w(t)}{4h^3(t)} (R^2 - r^2) \quad (16)$$

with $p(R, t) = 0$. The integrated vertical force due to the pressure distribution within $r = R$ is given by

$$F(R, t) = \int_0^R 2\pi r p(r, t) dr = \frac{3\pi \mu w(t) R^4}{8 h^3(t)}. \quad (17)$$

In our problem, however, h is a function of r and the pressure can be expressed as

$$p(r, t) = \int_R^r \frac{\partial p}{\partial \tilde{r}}(\tilde{r}, t) d\tilde{r}, \quad (18)$$

with $p(R, t) = 0$ and $\partial p / \partial \tilde{r}$ given by equation (15). The integrated vertical force $F(R, t)$ is still given by

$$F(R, t) = \int_0^R 2\pi r p(r, t) dr. \quad (19)$$

Using $h(r, t)$ from our simulations, we can calculate $F(R, t)$ according to equations (18) and (19) under the lubrication approximation. The integrated vertical force $F(R, t)$ so obtained is then compared to the corresponding numerical result $F_N(R, t) = \int_0^R 2\pi r [P(r, t) - P(R, t)] dr$, in which $P(r, t)$ is the pressure in the numerical simulations. This is to verify if our simulation results agree with the predictions of the lubrication approximation.

B. Numerical results

In our simulation, a gas bubble of diameter $D = 3.335$ mm is initially placed 15 mm below the solid wall which is 95% glycerin+water. The liquid density is $\rho = 1244$ kg/m³, and the viscosity is $\mu = 0.5501$ Pa · s. The diameter of our cylindrical computational domain is 40 times of the diameter of the gas bubble. The parameter values used here are different from those in sections III and IV. This is to help our simulations quickly enter into the regime of thin film dynamics. The distance between the wall and the center of the upper surface of the bubble is $h(r = 0, t)$. The thickness at the thinnest point of the film is denoted by $h_{\min}(t)$. The bubble is released at time $t = 0$. Figure 8 shows that when t is small, h_{\min} occurs at $r = 0$, i.e., $h(r = 0, t) = h_{\min}(t)$. As time goes by, the thinnest point of the liquid film moves outward and the upper surface of the bubble acquires a concave shape (see Figure 9 for the thin film at $t \approx 20$ s).

Figure 10(a) shows the time variation of the film thickness, with the blue line representing $h_{\min}(t)$ and the red stars representing $h(r = 0, t)$. The bubble rises very fast in the first second, and then slows down. This is also observed in figure 10(b) for $\frac{\partial}{\partial t} h_{\min}(t)$ and $\frac{\partial}{\partial t} h(r = 0, t)$. After time $t = 27$ s (at which $h_{\min} = 7.27 \times 10^{-3}$ mm, $h(r = 0) = 4.07 \times 10^{-2}$ mm), the computation breaks down. It will be shown below that for time t between $t_l = 3.7$ s and $t_u = 25$ s, good agreement can be achieved between the simulation results and the predictions of

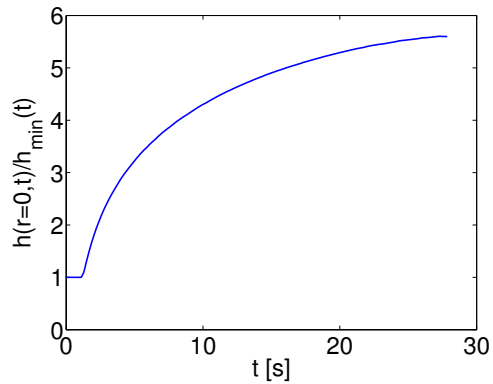


FIG. 8. The ratio of $h(r = 0, t)$ to $h_{\min}(t)$, $h(r = 0, t)/h_{\min}(t)$, plotted as a function of time t . As t increases, the thinnest point of the liquid film moves away from $r = 0$.

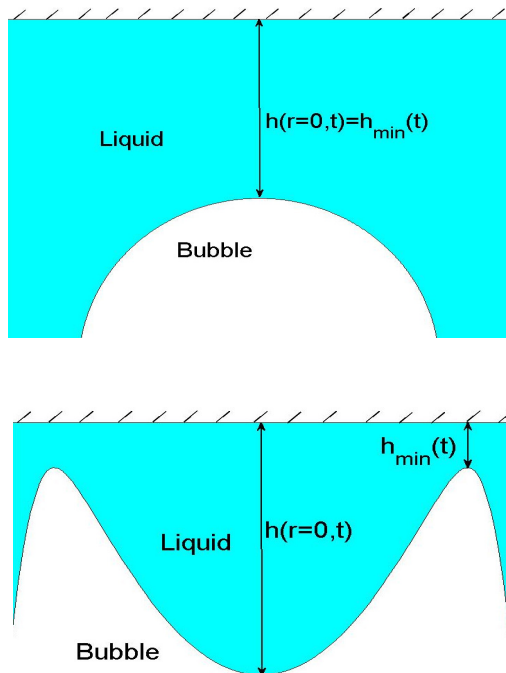
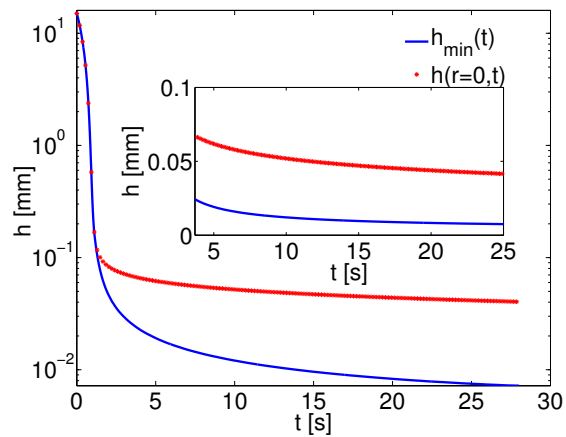


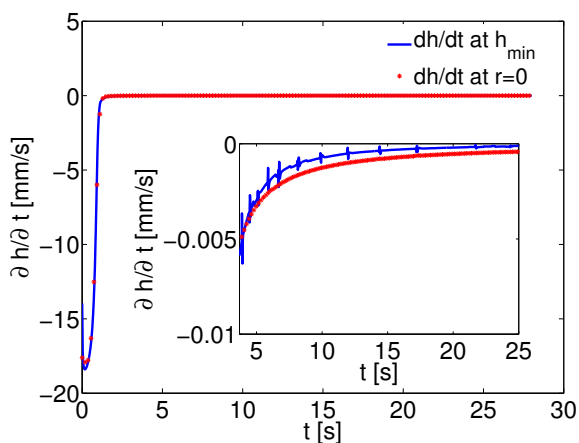
FIG. 9. The shape of the liquid film between the bubble and the wall. Upper: The bubble is far from the wall and h_{\min} occurs at $r = 0$. Lower: At $t \approx 20$ s, h_{\min} occurs at the neck.

the lubrication approximation. We note that there exist some sudden jumps in the curves for $\partial h / \partial t$. They correspond to the time instants of remeshing by which numerical errors are introduced.

As the film is very thin (from several microns to several tens of microns), the pressure P in the thin film is almost independent of z according to the lubrication approximation. In figure 11(a), we plot the pressure in the film as a function of r at $t \approx 20$ s. It can be observed that the pressure shows a sharp drop near the neck, i.e., $|\frac{\partial P}{\partial r}|$ is very



(a)

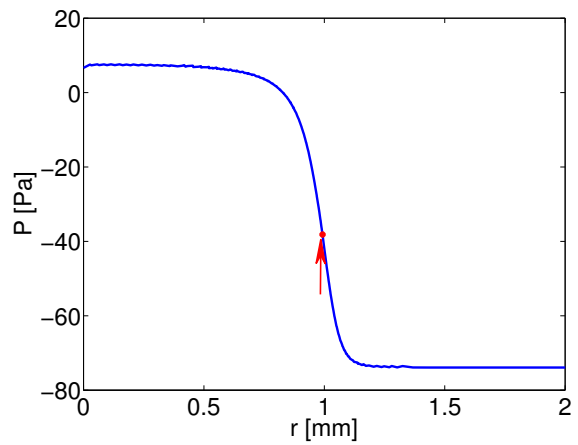


(b)

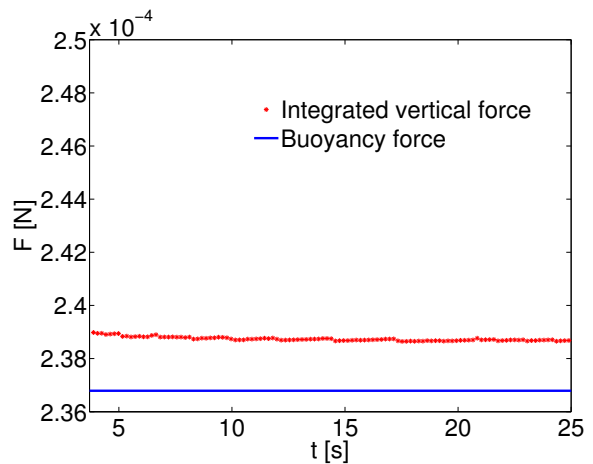
FIG. 10. (a) Film thickness h plotted as a function of t . The blue line represents $h_{\min}(t)$ and the red stars represent $h(r=0, t)$. For $t \leq 1.13$ s, $h_{\min}(t) = h(r=0, t)$. For $t > 1.13$ s, h_{\min} occurs at the neck which moves outward gradually. The difference between $h_{\min}(t)$ and $h(r=0, t)$ is shown in the inset with a better resolution. (b) The rate of change of h , $\partial h/\partial t$, plotted as a function of t for $h_{\min}(t)$ and $h(r=0, t)$.

large. The neck formation and the sharp drop of pressure at the neck are expected in the asymptotics of thin film dynamics. The pressure changes slowly with r far away from the neck and approaches a constant when r is big enough. This is because the liquid is almost in a hydrostatic state far away from the film, with a negligibly small flux of liquid escaping from the film. Using the numerical results for the pressure $P(r, t)$, we compute the integrated vertical force $F(\infty, t) = \int_0^\infty [P(r, t) - P(\infty, t)] 2\pi r dr$ on the bubble due to P . Figure 11(b) compares $F(\infty, t)$ and the buoyancy force $F_B = \rho g (\frac{4\pi}{3} R^3)$, which are approximately equal, with a relative error below 1%.

Finally we make comparison for the integrated vertical force. We compare the numerical result $F_N(R, t)$ with the prediction of the lubrication approximation $F(R, t)$. The



(a)



(b)

FIG. 11. (a) Pressure in the thin film, plotted as a function of r . Here the pressure value at r is obtained by averaging over the film thickness. The arrow points to the data point at the neck where the pressure drops sharply. Note that there is no pressure variation beyond $r = 2$ mm. (b) The integrated vertical force $F(\infty, t)$ numerically calculated and the buoyancy force F_B are approximately equal, with a relative error below 1%.

numerical result $F_N(R, t)$ is computed by using equation (19) with $p(r, t)$ replaced by $P(r, t) - P(R, t)$ obtained from the simulation. When R is selected at a circle close to the neck, $|\frac{\partial P}{\partial r}|$ at $r = R$ is very large, and hence a small change in R will result in a big shift of $P(R, t)$, which is taken as the reference point in $P(r, t) - P(R, t)$. So we choose R a bit away from the neck. The prediction of the lubrication approximation $F(R, t)$ can be calculated by using $h(r, t)$ obtained from the simulation and equations (8), (18) and (19). Figure 12 shows the relative error $E(t)$ between the numerical result $F_N(R, t)$ and the prediction of the lubrication approximation $F(R, t)$, with $E(t)$ given by

$$E(t) = \frac{F(R, t) - F_N(R, t)}{F_N(R, t)} \quad (20)$$

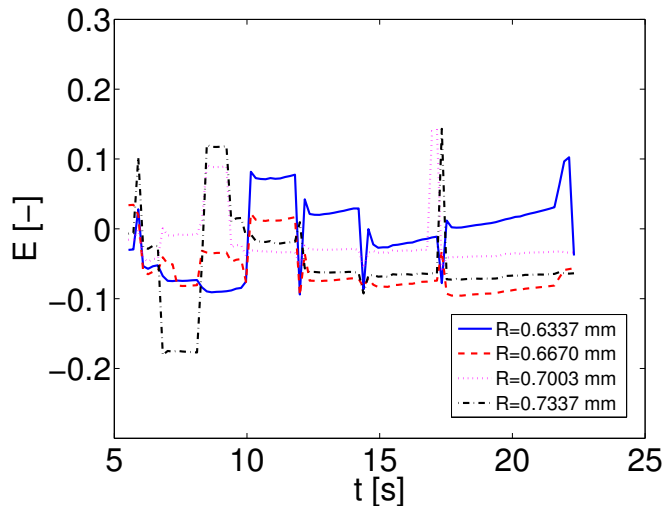


FIG. 12. The relative error $E(t)$ between the numerical result $F_N(R, t)$ and the prediction of the lubrication approximation $F(R, t)$ for the integrated vertical force. Results are shown for different values of R away from the neck. Here the sudden jumps correspond to the time instants of remeshing.

for four different values of R .

VI. CONCLUSIONS

We have numerically investigated a rising bubble interacting with a solid wall. This is carried out by employing an Arbitrary Lagrangian-Eulerian method on an adaptive moving mesh. In order to accurately approximate the boundary condition, the interface is composed of mesh lines, hence our method is an interface-conforming method. Finite element method is used to discretize the governing equations and the Uzawa algorithm is applied to solve the discrete system. We consider a bubble that is driven by the buoyancy force in a viscous liquid and rises toward a horizontal wall, with possible “approach-bounce” cycles. We start from a quantitative validation of our simulation by comparing the numerical results with experimental data for a bubble which reaches its terminal velocity before the impact on the wall. We then identify four distinct behaviors for the bubble dynamics governed by the competition among the inertial, viscous, gravitational, and capillary forces. We produce a phase diagram with the Ohnesorge number and Bond number acting as the two dimensionless control parameters. We finally investigate the late stage of the bubble rise characterized by a thinning liquid film between the wall and bubble. Comparing the simulation results with the predictions of the lubrication approximation for thin film dynamics, we obtain remarkable agreement to further demonstrate the accuracy of the simulations.

ACKNOWLEDGEMENT

This work is partially supported by Hong Kong RGC Collaborative Research Fund (No. C1018-17G).

- ¹S. POPINET and S. ZALESKI, “Bubble collapse near a solid boundary: a numerical study of the influence of viscosity,” *Journal of Fluid Mechanics* **464** (2002), 10.1017/s002211200200856x.
- ²K. Yokoi, D. Vellido, J. Hinch, and I. Hutchings, “Numerical studies of the influence of the dynamic contact angle on a droplet impacting on a dry surface,” *Physics of Fluids* **21**, 072102 (2009).
- ³P. C. Duineveld, “The rise velocity and shape of bubbles in pure water at high Reynolds number,” *Journal of Fluid Mechanics* **292**, 325 (1995).
- ⁴M. Wu and M. Gharib, “Experimental studies on the shape and path of small air bubbles rising in clean water,” *Physics of Fluids* **14**, L49 (2002).
- ⁵H.-K. Tsao and D. L. Koch, “Observations of high Reynolds number bubbles interacting with a rigid wall,” *Physics of Fluids* **9**, 44–56 (1997).
- ⁶E. Klaseboer, J.-P. Chevaillier, A. Maté, O. Masbernat, and C. Gourdon, “Model and experiments of a drop impinging on an immersed wall,” *Physics of Fluids* **13**, 45–57 (2001).
- ⁷D. Legendre, C. Daniel, and P. Guiraud, “Experimental study of a drop bouncing on a wall in a liquid,” *Physics of Fluids* **17**, 097105 (2005).
- ⁸R. Zenit and D. Legendre, “The coefficient of restitution for air bubbles colliding against solid walls in viscous liquids,” *Physics of Fluids* **21**, 083306 (2009).
- ⁹D. Kosior, J. Zawala, and K. Malysa, “Influence of n-octanol on the bubble impact velocity, bouncing and the three phase contact formation at hydrophobic solid surfaces,” *Colloids and Surfaces A: Physicochemical and Engineering Aspects* **441**, 788–795 (2014).
- ¹⁰T. Qin, S. Ragab, and P. Yue, “Axisymmetric simulation of the interaction of a rising bubble with a rigid surface in viscous flow,” *International Journal of Multiphase Flow* **52**, 60–70 (2013).
- ¹¹A. Albadawi, D. Donoghue, A. Robinson, D. Murray, and Y. Delauré, “On the assessment of a VOF based compressive interface capturing scheme for the analysis of bubble impact on and bounce from a flat horizontal surface,” *International Journal of Multiphase Flow* **65**, 82–97 (2014).
- ¹²E. Klaseboer, R. Manica, M. H. W. Hendrix, C.-D. Ohl, and D. Y. C. Chan, “A force balance model for the motion, impact, and bounce of bubbles,” *Physics of Fluids* **26**, 092101 (2014).
- ¹³R. Manica, E. Klaseboer, and D. Y. C. Chan, “Force balance model for bubble rise, impact, and bounce from solid surfaces,” *Langmuir* **31**, 6763–6772 (2015).
- ¹⁴R. Bonhomme, J. Magnaudet, F. Duval, and B. Piar, “Inertial dynamics of air bubbles crossing a horizontal fluid–fluid interface,” *Journal of Fluid Mechanics* **707**, 405–443 (2012).
- ¹⁵M. Manga and H. A. Stone, “Low Reynolds number motion of bubbles, drops and rigid spheres through fluid–fluid interfaces,” *Journal of Fluid Mechanics* **287**, 279 (1995).
- ¹⁶K. Singh and H.-J. Bart, “Passage of a single bubble through a liquid–liquid interface,” *Industrial & Engineering Chemistry Research* **54**, 9478–9493 (2015).
- ¹⁷S. G. Yiantsios and R. H. Davis, “On the buoyancy-driven motion of a drop towards a rigid surface or a deformable interface,” *Journal of Fluid Mechanics* **217**, 547 (1990).
- ¹⁸H. Power, “The interaction of a deformable bubble with a rigid wall at small Reynolds number: A general approach via integral equations,” *Engineering Analysis with Boundary Elements* **19**, 291–297 (1997).
- ¹⁹R. Clift, J. Grace, and M. Weber, *Bubbles, Drops, and Particles*, Dover Civil and Mechanical Engineering Series (Dover Publications, 2005).
- ²⁰M. Ohta, T. Imura, Y. Yoshida, and M. Sussman, “A computational study of the effect of initial bubble conditions on the

- motion of a gas bubble rising in viscous liquids,” *International Journal of Multiphase Flow* **31**, 223–237 (2005).
- ²¹G. Tryggvason, B. Bunner, A. Esmaeeli, D. Juric, N. Al-Rawahi, W. Tauber, J. Han, S. Nas, and Y.-J. Jan, “A front-tracking method for the computations of multiphase flow,” *Journal of Computational Physics* **169**, 708–759 (2001).
- ²²M. Sussman, P. Smereka, and S. Osher, “A level set approach for computing solutions to incompressible two-phase flow,” *Journal of Computational Physics* **114**, 146–159 (1994).
- ²³Z. Yu and L.-S. Fan, “Direct simulation of the buoyant rise of bubbles in infinite liquid using level set method,” *The Canadian Journal of Chemical Engineering* **86**, 267–275 (2008).
- ²⁴P. Yue, C. Zhou, J. J. Feng, C. F. Ollivier-Gooch, and H. H. Hu, “Phase-field simulations of interfacial dynamics in viscoelastic fluids using finite elements with adaptive meshing,” *Journal of Computational Physics* **219**, 47–67 (2006).
- ²⁵A. Fakhari, M. Geier, and T. Lee, “A mass-conserving lattice boltzmann method with dynamic grid refinement for immiscible two-phase flows,” *Journal of Computational Physics* **315**, 434–457 (2016).
- ²⁶J. Étienne, E. Hinch, and J. Li, “A lagrangian–eulerian approach for the numerical simulation of free-surface flow of a viscoelastic material,” *Journal of Non-Newtonian Fluid Mechanics* **136**, 157–166 (2006).
- ²⁷H. Hu, “Direct simulation of flows of solid-liquid mixtures,” *International Journal of Multiphase Flow* **22**, 335–352 (1996).
- ²⁸H. H. Hu, N. Patankar, and M. Zhu, “Direct numerical simulations of fluid–solid systems using the arbitrary lagrangian–eulerian technique,” *Journal of Computational Physics* **169**, 427–462 (2001).
- ²⁹P. Yue, J. J. Feng, C. A. Bertelo, and H. H. Hu, “An arbitrary lagrangian–eulerian method for simulating bubble growth in polymer foaming,” *Journal of Computational Physics* **226**, 2229–2249 (2007).
- ³⁰J. Li, “An arbitrary lagrangian eulerian method for three-phase flows with triple junction points,” *Journal of Computational Physics* **251**, 1–16 (2013).
- ³¹F. Hecht, “Bamg: bidimensional anisotropic mesh generator,” *User Guide*. INRIA, Rocquencourt (1998).
- ³²J. R. Shewchuk, “Delaunay refinement algorithms for triangular mesh generation,” *Computational Geometry* **22**, 21–74 (2002).
- ³³L. A. Freitag and C. Ollivier-Gooch, “Tetrahedral mesh improvement using swapping and smoothing,” *International Journal for Numerical Methods in Engineering* **40**, 3979–4002 (1997).
- ³⁴L. Landau and E. Lifshitz, *Course of theoretical physics. vol. 6: Fluid mechanics* (Pergamon Press, Oxford, 1959).
- ³⁵D. Y. C. Chan, E. Klaseboer, and R. Manica, “Film drainage and coalescence between deformable drops and bubbles,” *Soft Matter* **7**, 2235–2264 (2011).
- ³⁶D. Y. Chan, E. Klaseboer, and R. Manica, “Theory of non-equilibrium force measurements involving deformable drops and bubbles,” *Advances in Colloid and Interface Science* **165**, 70–90 (2011).
- ³⁷H. Ding, P. D. Spelt, and C. Shu, “Diffuse interface model for incompressible two-phase flows with large density ratios,” *Journal of Computational Physics* **226**, 2078–2095 (2007).
- ³⁸P. Gresho and R. Sani, “Incompressible flow and the finite element method, vol. 2, isothermal laminar flow, 1020 pp,” (2000).
- ³⁹R. Scardovelli and S. Zaleski, “DIRECT NUMERICAL SIMULATION OF FREE-SURFACE AND INTERFACIAL FLOW,” *Annual Review of Fluid Mechanics* **31**, 567–603 (1999).
- ⁴⁰F. Suñol and R. González-Cinca, “Rise, bouncing and coalescence of bubbles impacting at a free surface,” *Colloids and Surfaces A: Physicochemical and Engineering Aspects* **365**, 36–42 (2010).